





**Mechanisms of frictional energy dissipation at graphene grain boundaries**Xiang Gao , Wengen Ouyang , Oded Hod ,\* and Michael Urbakh *Department of Physical Chemistry, School of Chemistry, The Raymond and Beverly Sackler Faculty of Exact Sciences and The Sackler Center for Computational Molecular and Materials Science, Tel Aviv University, Tel Aviv 6997801, Israel*

(Received 7 April 2020; revised 15 December 2020; accepted 16 December 2020; published 15 January 2021)

In light of the race towards macroscale superlubricity of graphitic contacts, the effect of grain boundaries on their frictional properties becomes of central importance. Here, we elucidate the unique frictional mechanisms characterizing topological defects along typical graphene grain boundaries that can vary from being nearly flat to highly corrugated, depending on the boundary misfit angle. We find that frictional energy dissipation over grain boundaries can originate from variations of compressibility along the surface, heat produced during defect (un)buckling events, and elastic energy storage in irreversible buckling processes. These may lead to atypical nonmonotonic dependence of the average friction on the normal load. The knowledge gained in the present study is an important step towards the understanding of frictional effects of extended grain boundaries.

DOI: [10.1103/PhysRevB.103.045418](https://doi.org/10.1103/PhysRevB.103.045418)**I. INTRODUCTION**

Structural superlubricity, the intriguing behavior of ultralow friction at incommensurate solid/solid crystalline interfaces, has emerged as a promising way toward efficient reduction of energy dissipation and wear at various length scales [1]. This phenomenon has been experimentally demonstrated in various contacts of pristine single-crystal layered materials, including nano- and microscale graphitic structures [2,3], graphene/*h*-BN heterojunctions [4–7], homogenous MoS<sub>2</sub> interfaces [8–10], graphene/MoS<sub>2</sub> heterojunctions [11], as well as other crystalline interfaces [12]. The common feature characterizing contacts of layered materials is their anisotropic structure consisting of covalently bonded layers coupled to each other via weaker dispersive interactions. A necessary condition to obtain such structural superlubricity is incommensurability between the rigid crystalline networks of the contacting surfaces. For homogeneous layered material junctions this can be fulfilled when the contacting surfaces are laterally rotated with respect to each other, thus avoiding frictional lock-in at the commensurate aligned configuration [1,2]. The latter state is eliminated in heterojunctions that possess mismatching lattice periodicity, providing superlubric behavior that is robust against interface reorientations [4–6].

The demonstration of superlubric behavior at the nano- and micro-scales has triggered scientific and engineering efforts aiming to extend its scope towards the macroscale [13–15]. Within the realm of layered materials interfaces, further scaling-up of structural superlubricity towards the macroscopic world is, nevertheless, challenged by the polycrystalline nature of layered materials at larger scales. At increasing contact dimensions, the contacting surfaces often exhibit a mosaic of randomly oriented grains that are

separated by grain boundaries (GBs) in the form of chains of dislocations [16]. The randomness of the grain orientations has the potential to eliminate frictional lock-in due to reduced interfacial commensurability thus promoting superlubric behavior [17,18]. However, the GBs typically induce large out-of-plane surface deformations [19–21] that may degrade or even completely eliminate superlubricity, as well as impact wear resistance [22]. Moreover, if the polycrystalline surface grain density is relatively uniform, the overall GB length will scale with surface area and hence their frictional effects are expected to scale with surface area as well, thus eliminating the sublinear scaling of superlubricity with contact surface area [23]. Therefore, understanding the effect of GBs on the frictional behavior of layered-material contacts is imperative for achieving superlubricity at large-scale interfaces. Prior to studying the complex frictional behavior of the entire mosaic structure [24,25], it is instructive to focus first on the effects of individual topological defects that constitute a single GB. This allows us to elucidate the mechanisms of energy dissipation induced by such topological barriers and identify the corresponding characteristic frictional signatures.

To this end, we adopt a model system of polycrystalline graphene [20,21,26–29] with a single GB that consists of a chain of pentagon-heptagon pair dislocations [see Fig. 1(a)]. To study the localized effect of one or a few adjacent GB dislocations we consider a small pristine trilayer graphene (TLG) flake sliding over a limited section of the entire GB [see Fig. 3(a)]. To allow for the application of an external load, the entire system is placed on a pristine Bernal (AB)-stacked bilayer graphene (BLG) substrate, whose lower layer is kept rigid. We first study the structural properties of GBs for various relative orientations of the contacting grains using a dedicated classical force field [30–34]. Then, we perform fully atomistic molecular dynamics simulations to study the frictional properties of the flake when sliding over individual GB dislocations under various normal loads and identify the mechanisms underlying their tribological behavior. Details

\*Corresponding author: odedhod@tauex.tau.ac.il

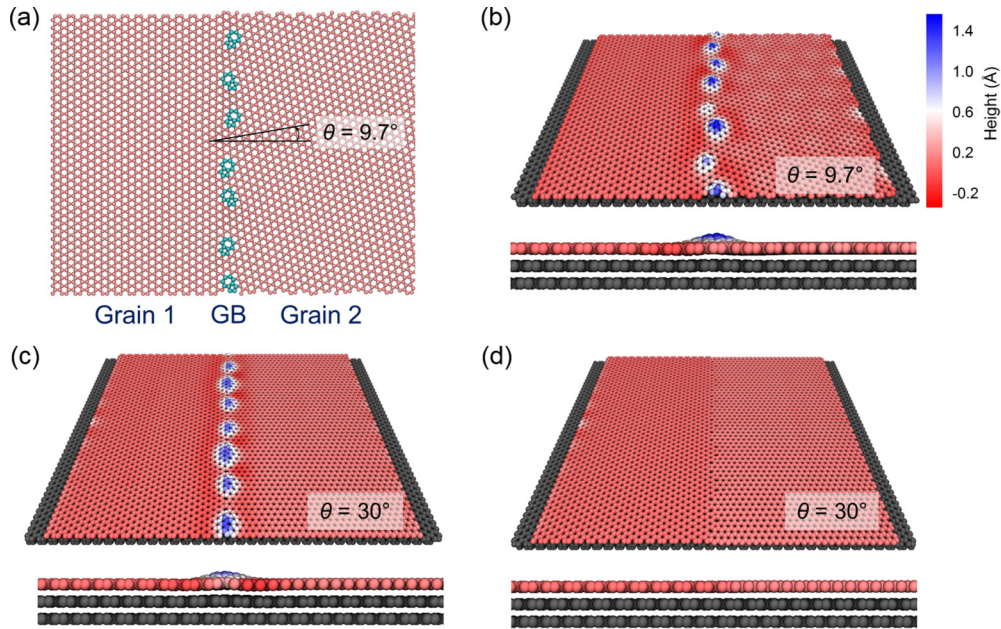


FIG. 1. Structure and topography of graphene GBs. (a) Atomic structure of a graphene GB with a misfit angle  $\theta = 9.7^\circ$ . The cyan and pink spheres represent the pentagon-heptagon dislocation atoms and hexagonal carbon atoms, respectively. (b)–(d) Perspective and cross-sectional views of graphene GBs on a BLG substrate with different misfit angles. (b) Corrugated GB with misfit angle  $\theta = 9.7^\circ$  (same GB as (a)). (c) Corrugated GB and (d) flat GB with the same misfit angle  $\theta = 30^\circ$ . The color of the spheres in the polycrystalline graphene layer in (b)–(d) represents the atomic height with respect to the average height of the two grains, using the color scale in (b). The grey spheres represent the carbon atoms of the pristine BLG substrate. The details for generating the configuration of graphene GB can be found in the Appendix.

regarding the structural relaxation and dynamic simulations are given in the Appendix.

## II. STRUCTURAL PROPERTIES OF GRAPHENE GRAIN BOUNDARIES

Graphene GBs typically consist of an array of pentagon-heptagon pair dislocations [see Fig. 1(a)], whose exact configuration is dictated by the relative orientation of the contacting grains (see Supplemental Material (SM) [35] Sec. 1 and Refs. [19,28,29] for further details). These topological defects lead to high local stress fields that can be relieved via out-of-plane surface deformation (see Fig. 1(b), SM [35] Sec. 2, and Ref. [30]). Since the substrate limits the possibility of downward protrusion, the local stresses developing at the GB are relieved via upward out-of-plane deformation. Such deformations have been experimentally characterized with both scanning tunneling microscopy (STM) and atomic force microscopy (AFM) [20,21]. Notably, the measured corrugation obtained by STM ( $\sim 8\text{--}15$  Å) is considerably larger than that measured by AFM ( $\sim 3$  Å). Hence, to better understand the relation between the orientation of the contacting grains and the structure of the GB, we studied a set of systems each consisting of two grains at different relative orientations. One of the grains (marked as “Grain 1”) is kept at AB stacking with the underlying pristine BLG substrate, whose armchair direction is placed along  $x$  axis. The orientation of the other grain (Grain 2) is varied in a counterclockwise direction with respect to the  $x$  axis to generate GBs of misfit angle,  $\theta$ , varying from  $0^\circ$  to  $60^\circ$  [see, e.g., Fig. 1(a)]. We note that due to the sixfold symmetry of the underlying pristine graphene

layer, this misfit angle range is complete. Following structural relaxation, two types of GBs are obtained: (i) Corrugated GBs that exhibit a series of upward protruded bumps along the GB, as shown in Figs. 1(b)–1(c). (ii) Flat GBs obtained for misfit angles in the range  $21.8^\circ < \theta < 38.2^\circ$  [see Fig. 1(d)] in agreement with experimental observations [21]. Specifically, we obtain such flat GBs for the angles  $\theta = 21.8^\circ$ ,  $25.7^\circ$ ,  $27.8^\circ$ , and  $30^\circ$  and their symmetric reflections around the  $30^\circ$  line. When analyzing the dependence of the topography and energetics of the GBs on the misfit angle, we find it necessary to further divide these GB types into two subgroups each (marked as Corrugated-I, Corrugated-II, Flat-I, and Flat-II). The different misfit angle dependence of each GB subgroup stems from the specific configuration of the corresponding GB lattice dislocations (see SM [35] Sec. 3 and Refs. [19,21] for further details).

In the range  $0^\circ < \theta < 21.8^\circ$  only Corrugated-I GBs appear. For small misfit angles, a bump height of  $\sim 2.2$  Å is obtained [see Fig. 2(a)] in good agreement with the experimental AFM observations [20,21]. When increasing the misfit angle in the range  $0^\circ < \theta < 12.5^\circ$ , we observe a rapid increase in the dislocation density [Fig. 2(b)] in accordance with theoretical predictions [19,36]. This induces stress cancellation between neighboring dislocations leading to a substantial decrease of the maximum bump height (from 2.2 Å to about 1.4 Å) with misfit angle up to  $\theta = 12.5^\circ$  [see Fig. 2(a)]. The combined effect of this structural behavior results in a rapid increase in the GB energy [see Fig. 2(c)] relative to the energy of the corresponding separated grains (see SM [35] Sec. 4 and Refs. [19,28] for further details on the GB energy calculation). In the subrange of  $12.5^\circ < \theta < 21.8^\circ$  the density of

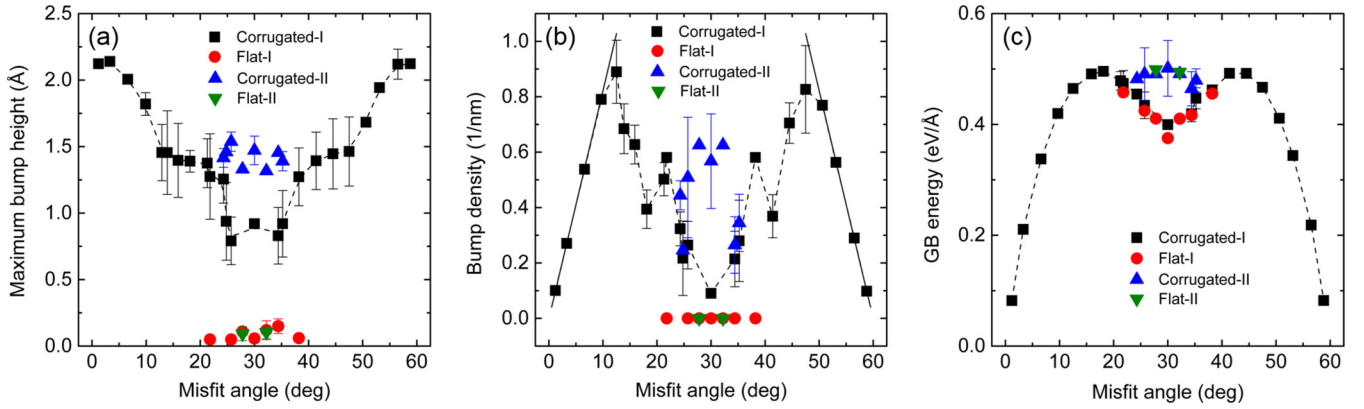


FIG. 2. Structure and energetics of graphene GBs. (a) Maximum bump height; (b) Graphene GB bump density; and (c) GB energy plotted as a function of misfit angle  $\theta$ . Based on the corrugation and the types of dislocations, the GBs are categorized in four groups: Corrugated-I (black squares), Corrugated-II (blue up triangles), Flat-I (red circles), and Flat-II (green down triangles). See SM [35] Secs. 1 and 3 for further details regarding the various GB types. The black solid lines in (b) indicate the theoretical prediction [19,36]. The black dashed lines in all panels are plotted to guide the eye. For flat GBs, the bump density is presented as zero and the maximum out-of-plane corrugation is shown in (a). Details regarding the estimation of the error bars can be found in the Appendix. Error bars smaller than the symbol size are not shown.

the Corrugated-I GB bumps generally reduces and their maximum height shows merely weak  $\theta$  dependence resulting in a mild reduction of the overall GB energy. Within this range, the dislocations tend to share a C-C bond, a hexagon carbon ring, or a pair of mutual edge atoms, which significantly reduces the local stress field and annihilates bumps. Finally, the  $21.8^\circ < \theta < 30^\circ$  GBs form quasi- or fully continuous dislocation chains (see SM [35] Sec. 3 and Refs [19,21]) of either Corrugated-I, Corrugated-II, or flat types. The Corrugated-II GBs show weak bump density and height dependence on the misfit angle as compared to the Corrugated-I subgroup that exhibits further density and height reduction [Figs. 2(a) and 2(b)]. Notably, the maximum out-of-plane corrugation of the flat GBs of both types is below 0.2 Å, which is significantly lower than that of the corrugated counterparts and is found to be independent of the misfit angle. At this misfit angle range, the difference in geometric structure of the various GBs leads to energetic splitting, where the Corrugated-I and Flat-I subgroups show reduction of GB energy with increased misfit angle, whereas the Corrugated-II and Flat-II subgroups show larger GB energy and weak  $\theta$  dependence [see Fig. 2(c)]. We note that the GB energies for the Corrugated-I and Flat-I GBs are comparable. This is because following structural relaxation, the GB energy is mainly determined by the dislocation types and densities. Since the Corrugated-I and Flat-I GBs share same type and similar dislocation density, their GB energies are comparable. A similar picture arises for the Corrugated-II and Flat-II GBs (see SM [35] Sec. 5 for further details).

### III. FRICTIONAL PROPERTIES OF GRAPHENE GRAIN BOUNDARIES

From the above analysis, we can expect that the frictional properties of interfaces consisting of polycrystalline graphene surfaces will depend on the relative orientation of the various grains. To gain microscopic understanding of the tribological effect of GBs, we considered three typical GBs of misfit angles  $4.7^\circ$ ,  $13.9^\circ$  and  $27.8^\circ$  that represent the low bump

density/high corrugation case, where the flake slides over a single bump; high bump density/low corrugation case, where the flake slides over two bumps; and flat GB topologies, respectively. Panels (a) and (b) of Fig. 3 show the setup for the friction simulations with the  $\theta = 4.7^\circ$  GB, where the TLG flake slides atop a bicrystalline graphene surface with a single GB supported by the pristine BLG substrate, whose lower layer is fixed. The slider is pulled from its optimal configuration by moving its top rigid layer with a constant velocity of 5 m/s across the GB (see the Appendix for further details). The frictional stress acting on the slider when crossing the GB is calculated as the average lateral force in the region near the GB divided by the flake's surface area. To avoid intractable computational burden, all simulations presented below are performed using a damped dynamics algorithm, i.e., Langevin dynamics at zero temperature [37]. Exemplary simulations performed at room temperature provide similar results (see SM [35] Sec. 7).

To estimate the friction coefficient associated with crossing the GB, we calculate the dependence of the frictional stress on the normal load applied to the upper rigid layer of the slider. Figure 3(c) presents the frictional stress obtained for the three GBs considered at the forward sliding direction (from Grain 1 to Grain 2, as noted in Fig. 1) compared to the pristine graphene surface results. All three representative GBs considered show an increase of the frictional stress with applied normal load, which is considerably steeper than that of the corresponding pristine surface. Notably, the two corrugated GBs ( $\theta = 4.7^\circ$ ,  $13.9^\circ$ ) show a sharp jump in the frictional stress at low normal loads, which is absent in the flat GB case ( $27.8^\circ$ ). At higher loads, the frictional stresses of the three GBs behave qualitatively similar, showing a linear increase with normal load.

The different behavior of the corrugated and flat GBs at the low normal load regime results from bump buckling and unbuckling processes that occur when sliding over corrugated GBs. To demonstrate this, we consider the  $\theta = 4.7^\circ$  GB and plot the corresponding lateral force traces [Fig. 4(a)] and the variations of the bump height and its vertical velocity

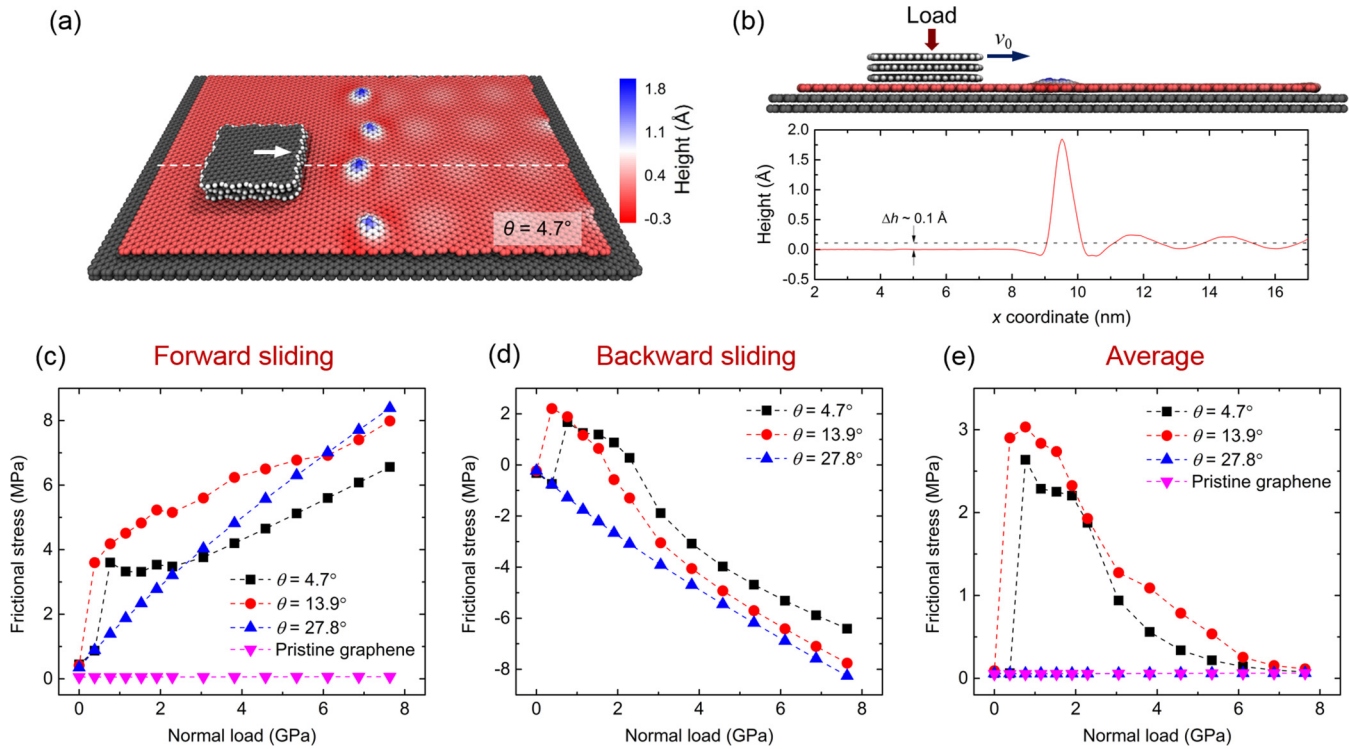


FIG. 3. Sliding simulation setup for a graphene flake over a graphene GB. (a) Schematic representation of the simulation setup for a TLG flake sliding over a GB of misfit angle  $\theta = 4.7^\circ$ . Polycrystalline substrate atoms are colored according to their vertical height. The grey and white spheres in other layers represent carbon and hydrogen atoms, respectively. The white dashed line depicts the scan line and the arrow shows the forward sliding direction. (b) Top: side view of the sliding system presented in panel (a); Bottom: the height profile along the white dashed scan line shown in panel (a) in absence of the flake. The black dashed line in (b) indicates the average height of Grain 2. (c)–(e) show the frictional stress as a function of normal load for the  $\theta = 4.7^\circ$  (black squares),  $13.9^\circ$  (red circles), and  $27.8^\circ$  (blue upper triangles) GBs in the forward and backward sliding directions and their average, respectively. Results obtained for a pristine graphene surface are presented for comparison by the magenta lower triangle symbols in panels (c) and (e). The dashed lines in (c)–(e) are plotted to guide the eye. More details regarding the friction calculations and the effect of scan-line position can be found in the Appendix, Sec. 7 and SM [35] Sec. 6, respectively. Movies of typical simulations are also provided in the SM [35].

[Fig. 4(b)] for three normal loads, corresponding to the different regimes discussed above. Starting at steady state over the left grain, the lateral force trace shows a resistive contribution when encountering the GB at zero normal load (see SM [35] Movie 1). This is associated with a mild ( $\sim 1 \text{ \AA}$ ) depression of the bump height. During the entire crossing process, the bump remains depressed and the lateral force shows somewhat enhanced oscillations. When the slider approaches the edge of the GB, the bump recovers resulting in an assistive lateral force leading the flake towards a new steady-state sliding over Grain 2. Importantly, in this case the shear induced bump depression is nearly adiabatic as reflected by the minor variations obtained in the vertical velocity. This, in turn, results in the low frictional stress obtained for the load free case. When increasing the load to 0.8 GPa, the bump dynamics changes dramatically (see SM [35] Movie 2). While the force trace exhibits similar trends as those of the load-free case, pronounced buckling occurs during the crossing process, where the bump is suppressed below the surface while storing an elastic energy of 0.8 eV (see SM [35] Sec. 8 and Refs. [38–41]). Notably, while this buckling is associated with an energy barrier of  $\sim 0.9 \text{ eV}$ , the corresponding unbuckling process has a significantly lower barrier of  $\sim 0.1 \text{ eV}$ . This explains why many of our dynamical simulations exhibit reversible buckling and

release of the stored elastic energy. During these buckling and unbuckling processes sharp variations in the vertical velocity ( $\pm \sim 600 \text{ m/s}$ ) are observed, which translate into high energy dissipation and hence enhanced friction (see SM [35] Secs. 9 and 10). Notably, the vertical buckling velocity is two orders of magnitude larger than the sliding velocity (5 m/s) used in our simulations. Therefore, our dynamical results are found to be consistent with quasistatic simulations (see SM [35] Sec. 11), indicating that our findings are insensitive to the sliding velocity in this range. At higher normal loads (7.6 GPa), the magnitude of the vertical velocity bursts during buckling and unbuckling considerably diminishes (lying in the range of  $-60$  to  $+30 \text{ m/s}$ ) and the contribution of the buckling process to the friction reduces (see SM [35] Movie 3). Nevertheless, the overall frictional stress continues to grow in the high normal load regime, suggesting that another mechanism contributes to the energy dissipation.

To elucidate this extra mechanism, we characterized the potential energy difference when the flake resides over the two grains (see SM [35] Sec. 13). To circumvent buckling effects we considered only the flat GB case ( $\theta = 27.8^\circ$ ). In Fig. 5(a), we plot the flake (black squares), interfacial (red circles), and substrate (blue triangles) components of this potential energy difference as a function of the normal load. It is clearly

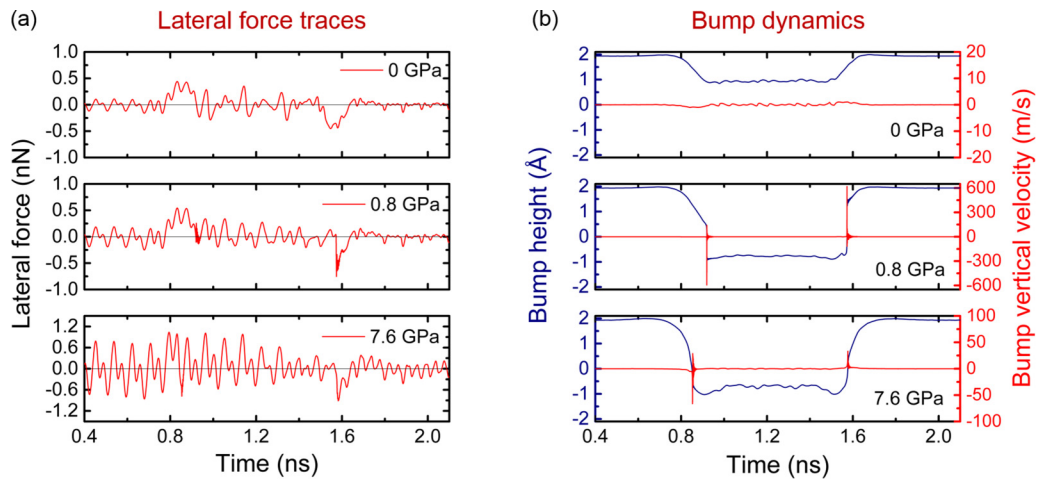


FIG. 4. Lateral force traces and bump dynamics of the  $\theta = 4.7^\circ$  GB in the forward sliding direction. (a) Lateral force traces as a function of time at different normal loads. (b) The height (purple) and vertical velocity (red) of the bump as a function of time. Results for normal loads of 0, 0.8, and 7.6 GPa are presented in the top, middle, and low panels, respectively. The highest atom of the bump peak at the initial configuration is chosen for the calculations of the bump height and vertical velocity at all simulation times. Additional results for lateral force traces and bump dynamics of the  $\theta = 4.7^\circ$ ,  $13.9^\circ$ ,  $27.8^\circ$  GBs and the pristine graphene substrate can be found in SM [35] Sec. 12. See SM [35] Movies 1–3 for the corresponding simulations of the  $\theta = 4.7^\circ$ .

evident that the main contribution to the pressure dependence of the potential energy difference during the GB crossing process originates from the substrate. Notably, with increasing normal load the barrier for the GB crossing process grows linearly. To further elucidate this effect, we plot in Fig. 5(b) the profile of the potential energy component associated with the substrate along the sliding path for various normal loads. Similar results for the other components can be found in SM [35] Sec. 13. We note that to reduce computational burden, these results were obtained by recording the corresponding potential energy contribution during a dynamical sliding simulation. We verified that this procedure faithfully represents results obtained via quasistatic calculations (see SM [35] Sec. 13). Notably, the pressure dependence of the substrate potential when the flake is located over Grain 2 is much more pronounced than for the case where the flake is located

over Grain 1. This can be attributed to the different stacking modes of the two grains over the underlying pristine graphene surface resulting in different compressibility behaviors. Here, one needs to distinguish between the commensurability of the lower flake layer and the two grains of the upper substrate layer, and the commensurability of the two grains with the underlying pristine substrate layers. In our  $\theta = 27.8^\circ$  GB model system, for example, the flake is incommensurate with both grains having average misfit angles of  $43.6^\circ$  and  $15.8^\circ$  with grains 1 and 2, respectively. Grain 1 is commensurate (AB stacking) with the bilayer graphene substrate, whereas Grain 2 is incommensurate with it. Under external normal loads, the interlayer distance decreases, pushing the system into the repulsive interlayer interactions regime. In the AB stacking characterizing Grain 1, half of the atomic centers of the grain overlap with the atoms of the underlying pristine

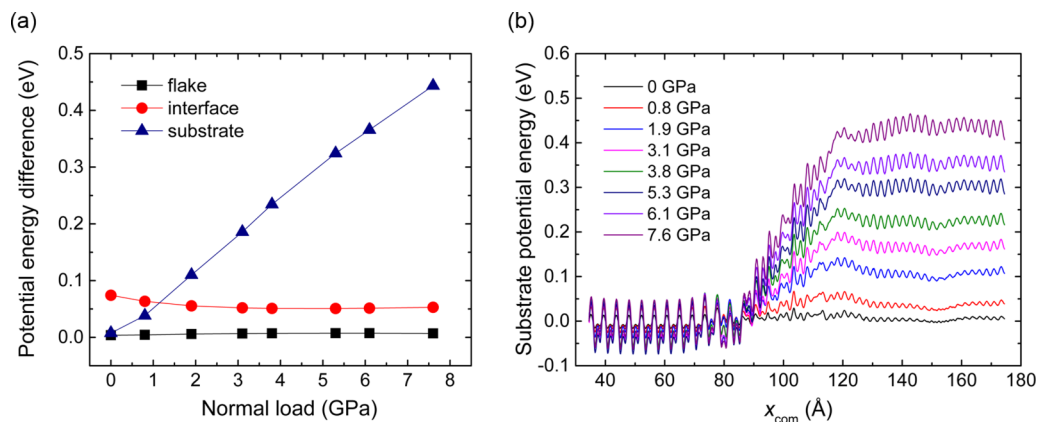


FIG. 5. Potential energy variations along the sliding path. (a) The flake (black squares), interfacial (red circles), and substrate (blue triangles) energy contributions to the potential energy difference when the flake is removed from Grain 1 and placed on Grain 2. (b) The potential energy profiles of the substrate for  $\theta = 27.8^\circ$  as a function of the displacement of the center of mass of the top layer of the sliding flake at different normal loads. For comparison purposes, the substrate potential energy under each normal load when the flake is positioned deep inside Grain 1 is set to zero.

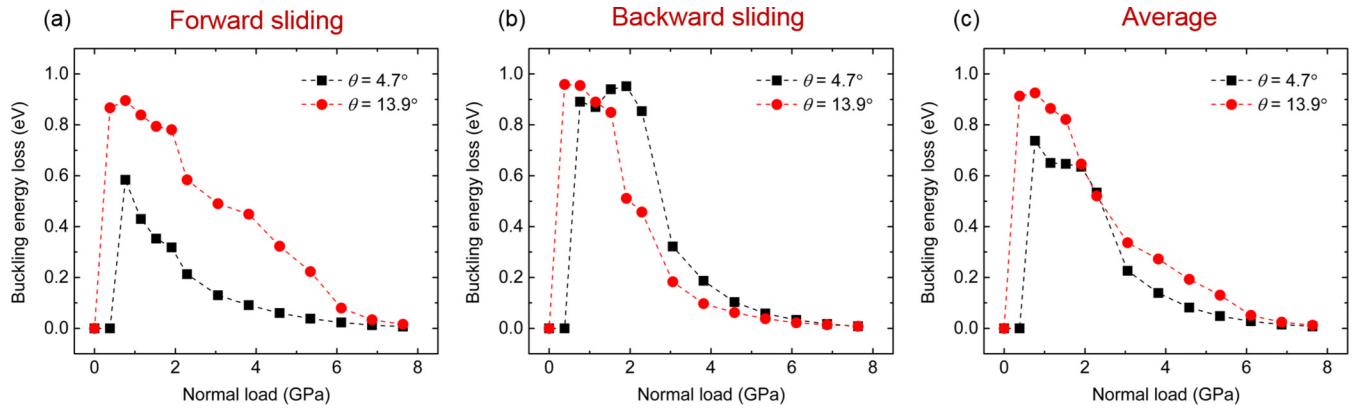


FIG. 6. Buckling energy dissipation for (a) forward sliding, (b) backward sliding, and (c) their average for the  $\theta = 4.7^\circ$  (black squares) and  $\theta = 13.9^\circ$  (red circles) GBs as a function of normal load. For normal loads below the buckling load, the energy loss associated with bump deformation is negligible and hence set to zero.

substrate layer. This leads to higher repulsive interactions and thus lower compressibility. Since Grain 2 is incommensurate with the middle substrate layer it experiences lower overlap between atomic positions and hence lower overall repulsive interactions and higher compressibility. A simple picture that rationalizes the potential response presented in Fig. 5(b) can be obtained by assuming harmonic behavior of the substrate response to the external load. In this simplified picture, Grain 1 has a higher spring constant than of Grain 2 ( $K_1 > K_2$ ). When the same load  $F$ , is applied to the two grains, their corresponding displacements are  $\Delta X_1 = F/K_1$  and  $\Delta X_2 = F/K_2$ , respectively. Plugging this into the expressions for the harmonic potential energy we get:  $U_1 = \frac{1}{2}K_1(\frac{F}{K_1})^2 = \frac{1}{2}\frac{F^2}{K_1}$  and similarly  $U_2 = \frac{1}{2}K_2(\frac{F}{K_2})^2 = \frac{1}{2}\frac{F^2}{K_2}$ . Therefore, we see that the potential energy is inversely proportional to the effective spring constant, and hence the potential energy response of Grain 1 to the external load is smaller than that of Grain 2. Consequently, with increasing pressure, the potential barrier needed to be crossed by the flake, when moving from Grain 1 to Grain 2, increases. This, in turn, leads to a linear increase in the friction force with the normal load resulting in a differential friction coefficient of 0.001 [calculated as the derivative of the  $\theta = 27.8^\circ$  (blue triangles) curve in Fig. 3(c)].

Importantly, this mechanism implies that when sliding over the GB in the opposite direction (from Grain 2 to Grain 1) the flake should experience an assistive force, whose magnitude increases with the normal load. A similar picture arises also for the corrugated GB systems discussed above, where bump buckling and grain compressibility effects are convolved. Therefore, in order to isolate the effect of the GB on the frictional properties of the system and to take into account that dynamic buckling can depend on the sliding direction we averaged the frictional stress obtained for the forward [see Fig. 3(c)] and backward [Fig. 3(d)] crossing process eliminating the grain compressibility contribution. This procedure corresponds well with typical friction experiments that measure multiple frictional loops [6,42,43]. Figure 3(e) presents the corresponding averaged frictional stresses as a function of normal load for the three GBs considered compared to a pristine substrate. The average friction experienced by the flake when crossing the flat GB is similar to that experienced

when sliding over pristine graphene. The two corrugated GB systems show a completely different behavior from that of the flat GB case. At the low normal load regime, the GB bumps are merely slightly deformed under the slider in a reversible manner resulting in very low energy dissipation. As the normal load increases, the average frictional stress rises sharply due to the shear induced buckling discussed above. The corresponding dissipated energy [see Fig. 6] has two contributions: (i) heat produced due to strong kinetic energy variations associated with the buckling process; and (ii) elastic energy stored in the buckled state. In case of unbuckling, the latter contribution can be partially recovered to produce an assistive force. Quantitatively, the former can be estimated from the kinetic energy pulses as shown in Fig. S11(a) of SM [35] Sec. 10, and the latter can be calculated from the potential energy profiles obtained by the nudged elastic band (NEB) calculations illustrated in SM [35] Sec. 8 (see also Refs. [38–41]). Above an external normal load of  $\sim 2$  GPa, the average frictional stress (after eliminating the potential gradient effect discussed above) gradually reduces with the external load approaching the frictional stress calculated over pristine graphene [see Fig. 3(e)]. This results from the fact that the vertical velocity bursts during the bump buckling and unbuckling process are suppressed by the external load and that buckling is found to be consistently reversible at this pressure regime. Overall, this behavior leads to the occurrence of negative average differential friction coefficients of the entire frictional loop [37].

We note that the average frictional dissipation associated with the crossing of the GB region results mainly from buckling/unbuckling processes, which primarily occur when the flake approaches or leaves the GB region, i.e., the stages, where the flake only partially covers the bump. In a certain range of normal loads, buckling/unbuckling of dislocations may also occur when the flake fully covers the bump. However, the magnitude of the energy dissipation during such buckling events is much smaller than in the former case. Hence, in the presence of buckling/unbuckling processes, the stages where the flake approaches or leaves the bump region contribute the most to the average frictional dissipation, whereas in the absence of buckling/unbuckling processes, the average friction is small throughout the dynamics [see Fig. 3(e)].

The frictional mechanisms described above significantly differ from topographic mechanisms previously discussed in the literature. The latter associate friction and assistive forces with physical atomic-scale steps encountered by the slider along the surface [44–46]. On the contrary, our findings suggest that, over corrugated GBs, friction may also originate from other sources including: (i) variations of compressibility along the surface, where different grains can store a different amount of elastic energy under the same normal load; (ii) heat produced during GB buckling and unbuckling events; and (iii) elastic energy storage in irreversible buckling processes. These unique mechanisms may lead to nonmonotonic dependence of the average friction on the normal load and the occurrence of negative average differential friction coefficients.

### ACKNOWLEDGMENTS

X.G. acknowledges the fellowship of the Sackler Center for Computational Molecular and Materials Science at Tel Aviv University. W.O. acknowledges financial support from the Planning and Budgeting Committee fellowship program for outstanding postdoctoral researchers from China and India in Israeli Universities and the support from the National Natural Science Foundation of China (Grants No. 11890673 and No. 11890674). O.H. is grateful for the generous financial support of the Israel Science Foundation under Grant No. 1586/17, Tel Aviv University Center for Nanoscience and Nanotechnology, and the Naomi Foundation for generous financial support via the 2017 Kadar Award. M.U. acknowledges the financial support of the Israel Science Foundation, Grant No. 1141/18 and the binational program of the National Science Foundation of China and Israel Science Foundation, Grant No. 3191/19.

### APPENDIX: METHODS

#### 1. Polycrystalline graphene model construction

The structures of polycrystalline graphene are generated by using a Voronoi tessellation method developed by Shekhawat [28,47], which creates physically realistic and low energy graphene GBs compared to the annealing method. Grain 1 is positioned such that its zigzag edge resides along the GB axis corresponding to an unrolled (0,1) nanotube of chiral angle  $\theta_1 = 30^\circ$  [see Fig. 1(a)]. Grain 2, is aligned such that its lattices corresponds to an unrolled  $(n_1, n_2)$  nanotube, where its chiral angle  $\theta_2 = \arctan[(2n_1 + n_2)/\sqrt{3}n_2]$  is varied to generate GBs of misfit angles ( $\theta = \theta_2 - \theta_1$ ) in the range of  $0^\circ - 60^\circ$ . The repeating unit cell along the GB axis has translation vectors of  $l_1 = \sqrt{3}a$  and  $l_2 = a\sqrt{3(n_1^2 + n_2^2 + n_1n_2)}$ , for Grain 1 and Grain 2 respectively, where  $a = 1.42039 \text{ \AA}$  is the equilibrium carbon-carbon bond length. The corresponding lattice vector of the supercell along this direction is chosen to reduce the strain magnitude  $|l_1q - l_2p|/|l_1q + l_2p|$  below  $10^{-3}$ , where  $p$  and  $q$  are the number of Grain 1 and Grain 2 duplicates in this direction within the supercell, respectively. To generate different GB configurations with the same misfit angle  $\theta$ , the grain dimension perpendicular to the GB

is appropriately adjusted. Following the Voronoi tessellation procedure and energy minimization of the interface, both flat and corrugated GB configurations are obtained.

#### 2. Grain boundary roughness calculations

To evaluate the roughness of the various GBs considered, the polycrystalline graphene surface was placed atop a pristine BLG substrate, which was taken to be periodic in both lateral directions with a supercell size of 6–20 nm along the GB axis and 10–20 nm in the perpendicular direction. The zigzag edge of the substrate was placed along the GB axis. The polycrystalline graphene layer was taken to be periodic along the GB direction, whereas open boundary conditions were applied to this layer in the perpendicular direction to allow for lateral deformation. To that end, the length of the polycrystalline graphene in the direction perpendicular to the GB axis was taken to be  $\sim 1.7 \text{ nm}$  shorter than the size of the box. The bottom layer of the BLG substrate was fixed rigidly during the calculation.

The geometry of the two top substrate layers was first optimized using the FIRE algorithm [48] with a force convergence criterion of  $10^{-3} \text{ eV/\AA}$ , followed by an annealing procedure, where the temperature was increased to 1000 K within 50 ps, maintained constant for 200 ps, and then cooled down to 0 K within 50 ps. Finally, the resulting structures were equilibrated for another 50 ps at 0 K. Here, the temperature of the system was controlled using Langevin dynamics with a damping coefficient of  $1 \text{ ps}^{-1}$  applied to the middle substrate layer. To avoid getting stuck in local minima configurations, if a depressed bump geometry appeared after the above-mentioned procedure, another annealing round was performed until all the bumps protruded upwards. For the analysis of the bump density appearing in Fig. 2(b), an out-of-plane corrugation threshold of  $0.5 \text{ \AA}$  was used to define the bump regions. The corresponding error bars in Fig. 2 were evaluated by calculating at least three different structures for each misfit angle.

#### 3. Sliding simulations

For sliding simulations performed at zero temperature, the polycrystalline graphene substrate was generated and annealed in the same way as that in the roughness calculations. A TLG flake of lateral dimension  $3.4 \times 3.2 \text{ nm}^2$ , with edge carbon atoms saturated by hydrogen atoms, was then placed atop Grain 1. To avoid a commensurate geometry, the orientation of the TLG flake was chosen to be rotated by  $43.6^\circ$  with respect to Grain 1 [exemplary geometry (xyz) files of the model systems are provided in the SM [35]]. A normal load was applied by imposing a constant force to each carbon atom in the top layer of the flake (which is kept rigid, flat, and parallel to the fixed lower substrate layer throughout the simulations) in the direction perpendicular to the surface. The magnitude of the normal force was varied in the range  $0 - 0.2 \text{ nN/atom}$ , corresponding to pressures of  $0 - 7.6 \text{ GPa}$ , which are typical for tribological experiments and simulations [5,37,49,50].

The geometry of the entire system (apart from the fixed bottom substrate layer and the rigid top flake layer) was

further optimized using the FIRE algorithm [48] with a force convergence criterion of  $10^{-3}$  eV/Å. Following the energy minimization, the flake was pulled by moving its top layer at a constant velocity of 5 m/s for 2.5 ns for GB misfit angles of  $\theta = 4.7^\circ$  and  $\theta = 13.9^\circ$ , and 2.8 ns for  $\theta = 27.8^\circ$ . Damped dynamics was applied to the atoms of the middle substrate layer and to the atoms of the middle flake layer with damping coefficients of  $1 \text{ ps}^{-1}$  acting in all directions of motion of each damped atom. In the sliding flake, damping was applied to atomic velocities relative to the center of mass motion. Furthermore, to reduce the effect of vertical oscillations of the entire flake an external damping force with  $1 \text{ ps}^{-1}$  damping coefficient was also added to each atom of the top layer of the flake along the vertical direction, as suggested in Ref. [51]. We verified that the results are insensitive to this choice of damping coefficient (see SM [35] Sec. 14). The friction force was then evaluated as minus the total instantaneous force exerted on the top layer of the flake.

To reduce computational burden the  $\theta = 4.7^\circ$  GB model was trimmed in the lateral directions and the dynamical simulations were performed with open boundary conditions. For  $\theta = 13.9^\circ$  and  $\theta = 27.8^\circ$  GBs, the polycrystalline graphene was kept periodic along the GB axis and open in the perpendicular (flake sliding) lateral direction.

For finite temperature simulations, the system was first equilibrated at 300 K using Langevin dynamics, then the flake was pulled along the same scan line as for the zero temperature simulations. Thermal averaging at each normal load value was done by performing three independent simulations with different initial conditions, generated consecutively during the equilibration simulations with 200 ps intervals.

We note that, apart from their effect on the frictional energy dissipation, grain boundary crossing may also induce wear [22]. In our simulations we use the reactive empirical bond order (REBO) intralayer potential that does allow for bond-breaking and formation within each layer. However, our interlayer potential does not allow for covalent bonding between the layers. Therefore, we are unable to simulate damage in the form of interlayer covalent bonding and are limited to intralayer defect formation. Having said that, we did not observe any irreversible damage or bond breaking of either the substrate or the slider up to a normal load of 7.8 GPa. We note that the fact that covalent bonds do not break within the layers, indicates that the chances of covalent interlayer bonding formation are very small, thus validating our simulation tools. It should be further noted that damage was observed under higher normal loads (12 GPa) in experiments involving graphene/Pt contacts [50]. Furthermore, recent simulations with sharp amorphous carbon tip models demonstrated wear at GBs under external loads exceeding 10 GPa [22].

#### 4. Quasistatic simulations

Validation static and quasistatic simulations were performed to ensure that the energy profile estimations performed via dynamical simulations faithfully represent the quasistatic results (see SM [35] Sec. 13). The static calculations were performed by placing the TLG flake at different positions along the sliding path and relaxing the system under an ex-

ternal normal load while freezing the lateral motion of the top TLG flake layer. The quasistatic calculations were performed using the protocol proposed Bonelli *et al.* [52]. We adopted the same system as that for the  $\theta = 27.8^\circ$  GB sliding simulations. The flake was initially positioned over Grain 1 (away from the GB region). At each step the top layer of the flake was rigidly displaced by  $0.2 \text{ Å}$  along the scan line towards Grain 2. The system was then relaxed (apart from the fixed bottom substrate layer and the rigid top flake layer) using the FIRE algorithm [48] with a force criterion of  $2 \times 10^{-3}$  eV/Å. Due to extremely heavy computation cost, the quasistatic simulations were performed only at a typical normal load of 3.8 GPa scanning over two chosen segments in the scan line, which correspond to the regions of Grain 1 and the GB, respectively. The comparison of the energy profiles obtained by the static, quasistatic, and dynamical simulation shows negligible differences thus justifying the use of dynamical simulations to calculate the energy profile.

The same quasistatic simulation scheme, with a force criterion of  $10^{-3}$  eV/Å, was adopted to verify that the buckling dynamics is independent of the sliding velocity in the velocity range considered (see SM [35] Sec. 11).

#### 5. Nudged elastic band calculations

To estimate the bump buckling energy barrier we performed NEB [38–41] calculations (shown in SM [35] Sec. 8) between the unbuckled and buckled bump states extracted from the sliding simulations. To this end, the flake was first removed from the buckled and unbuckled snapshots and the system was allowed to relax using the FIRE algorithm [48] with a force criterion of  $10^{-3}$  eV/Å. The resulting (local) minimum energy structures served as the initial and final structures for the NEB procedure and the buckling reaction coordinate was defined as per Ref. [53]. For the  $\theta = 13.9^\circ$  GB case, since there are intermediate states along the reaction path, the NEB calculations were performed in two steps, i.e., the reaction path between the first minimum and intermediate minimum, and the reaction path between the intermediate minimum and the final minimum.

#### 6. Additional simulation details

All simulations were performed using the LAMMPS package [54]. The intralayer and interlayer interactions were modeled with the second-generation REBO potential [55] and registry-dependent interlayer potential [31–34] with refined parameters [30], respectively. For roughness and sliding simulations, the time step used was 1 fs.

#### 7. Calculation of the friction force of GBs

The friction force is calculated by averaging the lateral force experienced by the top rigid layer of the TLG flake in a predefined region around the GB seam line. This region is defined as the region where the force trace deviates from its typical behavior deep inside the contacting grains. For example, a lateral force trace for the  $\theta = 4.7^\circ$  GB under zero normal load is shown in Fig. 7. The region between the dashed lines is defined as the GB region of width  $\sim 5.9 \text{ nm}$ . The same region is used for all the friction calculations under



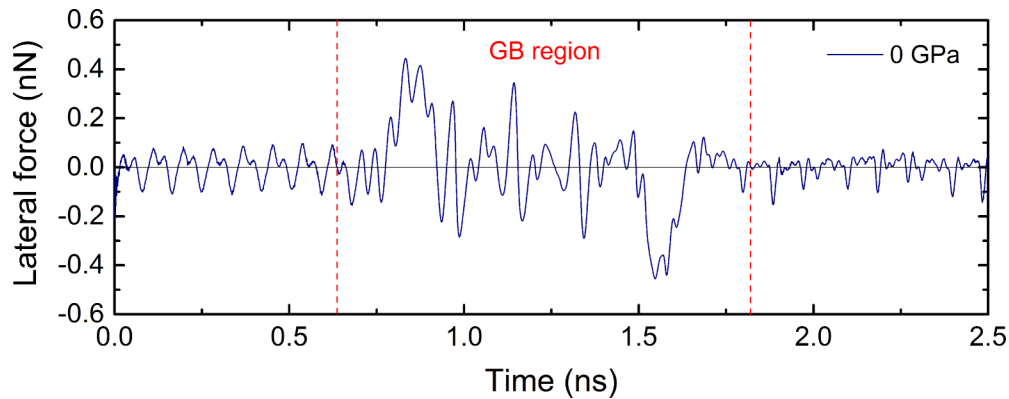


FIG. 7. GB region definition. An exemplary lateral force trace as a function of simulation time at zero normal load is presented for the  $\theta = 4.7^\circ$  GB. The red dashed lines mark the defined boundaries of the GB region.

different normal loads for both sliding directions. We note that the qualitative frictional behavior is not sensitive to the exact

choice of GB region. A similar procedure is used for all other GBs considered in this study.

- 
- [1] O. Hod, E. Meyer, Q. Zheng, and M. Urbakh, Structural superlubricity and ultralow friction across the length scales, *Nature (London)* **563**, 485 (2018).
- [2] M. Dienwiebel, G. S. Verhoeven, N. Pradeep, J. W. M. Frenken, J. A. Heimberg, and H. W. Zandbergen, Superlubricity of Graphite, *Phys. Rev. Lett.* **92**, 126101 (2004).
- [3] Z. Liu, J. Yang, F. Grey, J. Z. Liu, Y. Liu, Y. Wang, Y. Yang, Y. Cheng, and Q. Zheng, Observation of Microscale Superlubricity in Graphite, *Phys. Rev. Lett.* **108**, 205503 (2012).
- [4] I. Leven, D. Krepel, O. Shemesh, and O. Hod, Robust superlubricity in graphene/h-BN heterojunctions, *J. Phys. Chem. Lett.* **4**, 115 (2013).
- [5] D. Mandelli, I. Leven, O. Hod, and M. Urbakh, Sliding friction of graphene/hexagonal-boron nitride heterojunctions: A route to robust superlubricity, *Sci. Rep.* **7**, 10851 (2017).
- [6] Y. Song, D. Mandelli, O. Hod, M. Urbakh, M. Ma, and Q. Zheng, Robust microscale superlubricity in graphite/hexagonal boron nitride layered heterojunctions, *Nat. Mater.* **17**, 894 (2018).
- [7] Y. Liu, A. Song, Z. Xu, R. Zong, J. Zhang, W. Yang, R. Wang, Y. Hu, J. Luo, and T. Ma, Interlayer friction and superlubricity in single-crystalline contact enabled by two-dimensional flake-wrapped atomic force microscope tips, *ACS Nano* **12**, 7638 (2018).
- [8] J. M. Martin, C. Donnet, T. Le Mogne, and T. Epicier, Superlubricity of molybdenum disulphide, *Phys. Rev. B* **48**, 10583 (1993).
- [9] J. M. Martin, H. Pascal, C. Donnet, T. Le Mogne, J. L. Loubet, and T. Epicier, Superlubricity of MoS<sub>2</sub>: Crystal orientation mechanisms, *Surf. Coat. Technol.* **68–69**, 427 (1994).
- [10] H. Li, J. Wang, S. Gao, Q. Chen, L. Peng, K. Liu, and X. Wei, Superlubricity between MoS<sub>2</sub> monolayers, *Adv. Mater.* **29**, 1701474 (2017).
- [11] L. Wang, X. Zhou, T. Ma, D. Liu, L. Gao, X. Li, J. Zhang, Y. Hu, H. Wang, and Y. Dai, Superlubricity of a graphene/MoS<sub>2</sub> heterostructure: A combined experimental and DFT study, *Nanoscale* **9**, 10846 (2017).
- [12] M. Hirano, K. Shinjo, R. Kaneko, and Y. Murata, Observation of Superlubricity by Scanning Tunneling Microscopy, *Phys. Rev. Lett.* **78**, 1448 (1997).
- [13] D. Berman, S. A. Deshmukh, S. K. R. S. Sankaranarayanan, A. Erdemir, and A. V. Sumant, Macroscale superlubricity enabled by graphene nanoscroll formation, *Science* **348**, 1118 (2015).
- [14] D. Berman, A. Erdemir, and A. V. Sumant, Approaches for achieving superlubricity in two-dimensional materials, *ACS Nano* **12**, 2122 (2018).
- [15] M. I. De Barros Bouchet, J. M. Martin, J. Avila, M. Kano, K. Yoshida, T. Tsuruda, S. Bai, Y. Higuchi, N. Ozawa, M. Kubo *et al.*, Diamond-like carbon coating under oleic acid lubrication: Evidence for graphene oxide formation in superlow friction, *Sci. Rep.* **7**, 46394 (2017).
- [16] O. V. Yazyev and Y. P. Chen, Polycrystalline graphene and other two-dimensional materials, *Nat. Nanotechnol.* **9**, 755 (2014).
- [17] A. S. de Wijn, A. Fasolino, A. Filippov, and M. Urbakh, Low friction and rotational dynamics of crystalline flakes in solid lubrication, *EPL* **95**, 66002 (2011).
- [18] S.-W. Liu, H.-P. Wang, Q. Xu, T.-B. Ma, G. Yu, C. Zhang, D. Geng, Z. Yu, S. Zhang, W. Wang *et al.*, Robust microscale superlubricity under high contact pressure enabled by graphene-coated microsphere, *Nat. Commun.* **8**, 14029 (2017).
- [19] O. V. Yazyev and S. G. Louie, Topological defects in graphene: Dislocations and grain boundaries, *Phys. Rev. B* **81**, 195420 (2010).
- [20] J. Červenka and C. F. J. Flipse, Structural and electronic properties of grain boundaries in graphite: Planes of periodically distributed point defects, *Phys. Rev. B* **79**, 195429 (2009).
- [21] Y. Tison, J. Lagoute, V. Repain, C. Chacon, Y. Girard, F. Joucken, R. Sporcken, F. Gargiulo, O. V. Yazyev, and S. Rousset, Grain boundaries in graphene on SiC(0001 $\bar{1}$ ) substrate, *Nano Lett.* **14**, 6382 (2014).
- [22] J. Zhang, X. Chen, Q. Xu, T. Ma, Y. Hu, H. Wang, A. K. Tieu, and J. Luo, Effects of grain boundary on wear of graphene at the nanoscale: A molecular dynamics study, *Carbon* **143**, 578 (2019).

- [23] D. Dietzel, M. Feldmann, U. D. Schwarz, H. Fuchs, and A. Schirmeisen, Scaling Laws of Structural Lubricity, *Phys. Rev. Lett.* **111**, 235502 (2013).
- [24] A. Kavalur and W. K. Kim, Molecular dynamics study on friction of polycrystalline graphene, *Comput. Mater. Sci.* **137**, 346 (2017).
- [25] H. Li and W. K. Kim, Role of multigrain structure on friction of graphene layers, *Comput. Mater. Sci.* **165**, 23 (2019).
- [26] L. P. Biró and P. Lambin, Grain boundaries in graphene grown by chemical vapor deposition, *New J. Phys.* **15**, 035024 (2013).
- [27] P. Simonis, C. Goffaux, P. A. Thiry, L. P. Biro, P. Lambin, and V. Meunier, STM study of a grain boundary in graphite, *Surf. Sci.* **511**, 319 (2002).
- [28] C. Ophus, A. Shekhawat, H. Rasool, and A. Zettl, Large-scale experimental and theoretical study of graphene grain boundary structures, *Phys. Rev. B* **92**, 205402 (2015).
- [29] K. Kim, Z. Lee, W. Regan, C. Kisielowski, M. F. Crommie, and A. Zettl, Grain boundary mapping in polycrystalline graphene, *ACS Nano* **5**, 2142 (2011).
- [30] W. Ouyang, D. Mandelli, M. Urbakh, and O. Hod, Nanoserpents: Graphene nanoribbon motion on two-dimensional hexagonal materials, *Nano Lett.* **18**, 6009 (2018).
- [31] A. N. Kolmogorov and V. H. Crespi, Registry-dependent inter-layer potential for graphitic systems, *Phys. Rev. B* **71**, 235415 (2005).
- [32] I. Leven, I. Azuri, L. Kronik, and O. Hod, Inter-layer potential for hexagonal boron nitride, *J. Chem. Phys.* **140**, 104106 (2014).
- [33] I. Leven, T. Maaravi, I. Azuri, L. Kronik, and O. Hod, Interlayer potential for graphene/h-BN heterostructures, *J. Chem. Theory Comput.* **12**, 2896 (2016).
- [34] T. Maaravi, I. Leven, I. Azuri, L. Kronik, and O. Hod, Inter-layer potential for homogeneous graphene and hexagonal boron nitride systems: Reparametrization for many-body dispersion effects, *J. Phys. Chem. C* **121**, 22826 (2017).
- [35] See Supplemental Material at <http://link.aps.org/supplemental/10.1103/PhysRevB.103.045418> for additional information of structural properties of GBs, MD simulation details and results, NEB calculation results, energy dissipation analysis, exemplary geometry files, and movies of typical simulations.
- [36] J. P. Hirth and J. Lothe, *Theory of Dislocations* (Wiley, NY, 1982).
- [37] D. Mandelli, W. Ouyang, O. Hod, and M. Urbakh, Negative friction coefficients in superlubric graphite–Hexagonal Boron Nitride Heterojunctions, *Phys. Rev. Lett.* **122**, 076102 (2019).
- [38] G. Henkelman and H. Jónsson, Improved tangent estimate in the nudged elastic band method for finding minimum energy paths and saddle points, *J. Chem. Phys.* **113**, 9978 (2000).
- [39] G. Henkelman, B. P. Uberuaga, and H. Jónsson, A climbing image nudged elastic band method for finding saddle points and minimum energy paths, *J. Chem. Phys.* **113**, 9901 (2000).
- [40] A. Nakano, A space–time-ensemble parallel nudged elastic band algorithm for molecular kinetics simulation, *Comput. Phys. Commun.* **178**, 280 (2008).
- [41] E. Maras, O. Trushin, A. Stukowski, T. Ala-Nissila, and H. Jónsson, Global transition path search for dislocation formation in Ge on Si(001), *Comput. Phys. Commun.* **205**, 13 (2016).
- [42] A. Socoliuc, E. Gnecco, S. Maier, O. Pfeiffer, A. Baratoff, R. Bennewitz, and E. Meyer, Atomic-scale control of friction by actuation of nanometer-sized contacts, *Science* **313**, 207 (2006).
- [43] A. Socoliuc, R. Bennewitz, E. Gnecco, and E. Meyer, Transition from Stick-Slip to Continuous Sliding in Atomic Friction: Entering a New Regime of Ultralow Friction, *Phys. Rev. Lett.* **92**, 134301 (2004).
- [44] H. Hölscher, D. Ebeling, and U. D. Schwarz, Friction at Atomic-Scale Surface Steps: Experiment and Theory, *Phys. Rev. Lett.* **101**, 246105 (2008).
- [45] Z. Chen, A. Khajeh, A. Martini, and S. H. Kim, Chemical and physical origins of friction on surfaces with atomic steps, *Sci. Adv.* **5**, eaaw0513 (2019).
- [46] Z. Ye and A. Martini, Atomic friction at exposed and buried graphite step edges: Experiments and simulations, *Appl. Phys. Lett.* **106**, 231603 (2015).
- [47] A. Shekhawat and R. O. Ritchie, Toughness and strength of nanocrystalline graphene, *Nat. Commun.* **7**, 10546 (2016).
- [48] E. Bitzek, P. Koskinen, F. Gähler, M. Moseler, and P. Gumbsch, Structural Relaxation Made Simple, *Phys. Rev. Lett.* **97**, 170201 (2006).
- [49] M. M. van Wijk, M. Dienwiebel, J. W. M. Frenken, and A. Fasolino, Superlubric to stick-slip sliding of incommensurate graphene flakes on graphite, *Phys. Rev. B* **88**, 235423 (2013).
- [50] A. Klemenz, L. Pastewka, S. G. Balakrishna, A. Caron, R. Bennewitz, and M. Moseler, Atomic scale mechanisms of friction reduction and wear protection by graphene, *Nano Lett.* **14**, 7145 (2014).
- [51] W. Ouyang, M. Ma, Q. Zheng, and M. Urbakh, Frictional properties of nanojunctions including atomically thin sheets, *Nano Lett.* **16**, 1878 (2016).
- [52] F. Bonelli, N. Manini, E. Cadelano, and L. Colombo, Atomistic simulations of the sliding friction of graphene flakes, *Eur. Phys. J. B* **70**, 449 (2009).
- [53] Neb command — LAMMPS documentation, <https://lammmps.sandia.gov/doc/neb.html>.
- [54] S. Plimpton, Fast parallel algorithms for short-range molecular dynamics, *J. Comput. Phys.* **117**, 1 (1995).
- [55] D. W. Brenner, O. A. Shenderova, J. A. Harrison, S. J. Stuart, B. Ni, and S. B. Sinnott, A second-generation reactive empirical bond order (REBO) potential energy expression for hydrocarbons, *J. Phys.: Condens. Matter* **14**, 783 (2002).